

The Origin of Parity Violation in Polarized Dust Emission and Implications for Cosmic Birefringence

S. E. CLARK,¹ CHANG-GOO KIM,² J. COLIN HILL,^{3,4} AND BRANDON S. HENSLEY^{2,5}

¹*Institute for Advanced Study, 1 Einstein Drive, Princeton, NJ 08540, USA*

²*Department of Astrophysical Sciences, Princeton University, 4 Ivy Lane, Princeton, NJ 08544, USA*

³*Department of Physics, Columbia University, New York, NY, USA 10027*

⁴*Center for Computational Astrophysics, Flatiron Institute, New York, NY, USA 10010*

⁵*Spitzer Fellow*

ABSTRACT

Recent measurements of Galactic polarized dust emission have found a nonzero TB signal, a correlation between the total intensity and the B -mode polarization component. We present evidence that this parity-odd signal is driven by the relative geometry of the magnetic field and the filamentary interstellar medium in projection. Using neutral hydrogen morphology and Planck polarization data, we find that the angle between intensity structures and the plane-of-sky magnetic field orientation is predictive of the signs of Galactic TB and EB . Our results suggest that magnetically misaligned filamentary dust structures introduce nonzero TB and EB correlations in the dust polarization, and that the intrinsic dust EB can be predicted from measurements of dust TB and TE over the same sky mask. We predict correlations between TE , TB , EB , and EE/BB , and confirm our predictions using synthetic dust polarization maps from magnetohydrodynamic simulations. We introduce and measure a scale-dependent effective magnetic misalignment angle, $\psi_\ell^{dust} \sim 5^\circ$ for $100 \lesssim \ell \lesssim 500$, and predict a positive intrinsic dust EB with amplitude $\langle D_\ell^{EB} \rangle \lesssim 2.5 \mu\text{K}_{\text{CMB}}^2$ for the same multipole range at 353 GHz over our sky mask. Both the sign and amplitude of the Galactic EB signal can change with the sky area considered. Our results imply that searches for parity violation in the cosmic microwave background must account for the nonzero Galactic EB and TB signals, necessitating revision of existing analyses of the evidence for cosmic birefringence.

1. INTRODUCTION

The polarized sky at microwave frequencies consists, at minimum, of radiation from the cosmic microwave background (CMB) and dust and synchrotron emission from the Milky Way. On the celestial sphere, the observed Stokes Q and U parameters describing the linear polarization field can be decomposed into two rotationally invariant quantities that behave differently under a parity transformation: an E -mode component that does not change sign, and a B -mode component that does. This decomposition is motivated by the study of the polarized CMB, because scalar perturbations in the early universe generate only E -mode fluctuations at linear order, while tensor perturbations — a prediction of inflationary cosmology — generate both E - and B -mode fluctuations at the surface of last scatter-

ing (Kamionkowski et al. 1997b,a; Seljak & Zaldarriaga 1997).

The primordial B -mode polarization signal has not yet been detected, and is known to be subdominant at all frequencies to polarized Galactic emission across the full sky (e.g., Flauger et al. 2014; BICEP2/Keck Collaboration et al. 2015; Planck Collaboration Int. XXX 2016; BICEP2 Collaboration et al. 2018; Planck Collaboration XI 2020). At frequencies $\gtrsim 100$ GHz, the Galactic polarization is dominated by dust emission: partially polarized thermal emission from interstellar dust grains that are preferentially aligned with their short axes parallel to the ambient magnetic field (Purcell 1975). The E - and B -mode polarization from Galactic dust emission thus probe the magnetic interstellar medium (ISM). Characterizing this emission is important for understanding the interplay between matter and magnetic fields in the ISM, as well as for foreground mitigation for CMB experiments.

Statistical quantities of interest include the cross- or auto-power spectra of the polarized emission: C_ℓ^{XY} , which we will refer to with the shorthand XY , where X and Y are any of T (total intensity), E , and B . The Planck satellite mapped the whole sky in nine frequency bands, including seven that were sensitive to polarization (Planck Collaboration I 2020). These maps enable measurements of the polarized cross-power spectra of Galactic emission, particularly at 353 GHz, the highest-frequency polarization-sensitive Planck channel and the channel most sensitive to polarized dust emission. For the diffuse sky at 353 GHz the Planck data at large angular scales exhibit several statistical properties of note: an overall asymmetry in the amplitude of E - and B -mode power in the Galactic emission ($EE/BB \sim 2$), a positive cross-correlation between the total intensity and the E -mode polarization ($TE > 0$), and a weakly positive TB , the cross-correlation between total intensity and the B -mode polarization (Planck Collaboration Int. XXX 2016; Planck Collaboration XI 2020). EE , BB , and TE are invariant under a parity transformation, but this property is not shared by TB , the correlation between the scalar intensity and the parity-odd component of the polarization. EB is also a parity-odd quantity, but is consistent with null in the Planck data, within the statistical errors (Planck Collaboration XI 2020).

What is the physical origin of these statistical correlations? The possible relationship between these correlations and the turbulent properties of the ISM is an area of active study (Caldwell et al. 2017; Kandell et al. 2017; Kritsuk et al. 2018; Kim et al. 2019). Both the nonunity EE/BB and positive TE correlations are thought to originate, at least on some angular scales, from the preferential alignment between anisotropic density structures and the interstellar magnetic field (Clark et al. 2015; Planck Collaboration Int. XXXVIII 2016). This interpretation is strongly supported by investigations based on the structure of 21-cm neutral hydrogen (HI) emission. This line of inquiry began with the discovery that slender linear features in high-resolution HI maps are extremely well aligned with the ambient magnetic field as traced by starlight polarization (McClure-Griffiths et al. 2006; Clark et al. 2014) and polarized thermal dust emission (Clark et al. 2015; Martin et al. 2015). Indeed, template maps constructed solely from HI orientation and dust total intensity can reproduce the EE/BB asymmetry (Clark et al. 2015). The geometry of HI emission alone is predictive of a number of statistical properties of dust polarization, including the EE/BB ratio and positive TE correlation (Clark & Hensley 2019).

Similar phenomenology has not yet been observationally linked to the nonvanishing parity-odd TB correlation. While there is no *a priori* reason that the observed Galactic polarization must be parity invariant,¹ there is also no well-motivated physical model that predicted this parity violation, nor its observed scale dependence. As the ISM is sculpted by magnetohydrodynamic (MHD) turbulence, the TB signal could plausibly be related to some parity-odd MHD quantity, e.g., the magnetic helicity or cross-helicity (Brandenburg & Subramanian 2005; Blackman 2015). Toy models of a large-scale helical magnetic field can produce nonzero TB and TE signals at very low multipoles ($\ell < 22$; Bracco et al. 2019a), but the observed TB and TE spectra are much flatter than predicted by these models (Huffenberger et al. 2020).

The empirical relationship between magnetically aligned density structures and the TE and EE/BB correlations motivates consideration of a filament-based explanation for nonzero TB . Idealized filaments with polarized emission that is either parallel or perpendicular to the long axis of the filament will produce predominantly E -like polarization, while a 45° angle between the filament axis and the polarization angle preferentially generates B -like polarization (Zaldarriaga 2001; Rotti & Huffenberger 2019; Huffenberger et al. 2020). If filamentary dust emission is the correct model for production of both nonzero TE and nonzero TB , it implies a nonzero Galactic EB signal as well.

Measuring a nonzero EB correlation in the primary CMB would be evidence for parity-violating physics beyond the standard model of cosmology, such as cosmic birefringence (e.g., Carroll 1998), or of non-trivial symmetry-breaking properties in the physics of inflation (e.g., Watanabe et al. 2009, 2011; Dulaney & Gresham 2010). Imperfect calibration of the overall angle of a polarimeter will also generate nonzero EB ; a frequent practice is to correct for this systematic error by forcing EB to vanish (at CMB-dominated frequencies), under the hypothesis that the primordial $EB = 0$ (Yadav et al. 2010; Keating et al. 2013; Abitbol et al. 2016). This process, known as “self-calibration,” removes any sensitivity to an overall cosmic birefringence angle in the data, although the power spectrum of the birefringence fluctuations can still be constrained (Kaufman et al. 2014; Ade et al. 2015; BICEP2 Collaboration et al. 2017; Namikawa et al. 2020; Bianchini et al. 2020; Gruppuso et al. 2020). Alternatively, by using instrument model-

¹ Here we refer to the parity properties of the observed sky, which can be a particular realization of a parity-invariant underlying theory.

ing and/or *in situ* measurements, one can calibrate the polarimeter angle independently and thus constrain an overall cosmic birefringence angle via the observed EB and TB . The latest constraints from Planck (Planck Collaboration Int. XLIX 2016) and the Atacama Cosmology Telescope using this method find results consistent with null (Choi et al. 2020b).

The possibility of a nonzero Galactic EB signal further complicates attempts to measure a primordial EB correlation, as well as the self-calibration technique that assumes the intrinsic CMB EB and TB signals vanish (Abitbol et al. 2016). Minami et al. (2019) introduced a formalism for simultaneous determination of the instrument miscalibration and cosmic birefringence angles, taking advantage of the fact that the Galactic foreground polarization is rotated by the instrument miscalibration angle only, while the CMB polarization is rotated by both the miscalibration and the cosmic birefringence. Minami & Komatsu (2020) (hereafter MK20) used this methodology to find evidence for an isotropic cosmic birefringence angle β in Planck data at 2.4σ significance ($\beta = 0.35 \pm 0.14$), with the additional assumption that the Galactic $EB = 0$. If the Galactic EB is nonzero, the evidence for cosmic birefringence must be reevaluated in light of this foreground signal.

In this paper, we use information derived from HI data to present evidence that imperfect alignment between filamentary dust structures and the sky-projected magnetic field is the origin of nonzero TB and EB in the Galactic dust emission. In Section 2 we introduce the data used in this analysis. In Section 3 we demonstrate that the measurement of nonzero Galactic TB over the diffuse sky is robust. In Section 4, we describe our hypothesis for the origin of parity-odd quantities in dust polarization (4.1) and demonstrate support for our hypothesis in Planck data for the TB signal (4.2) and for the EB signal (4.3). We interpret these results in Section 4.4 and test further predictions of our model in both Planck data and MHD simulations in Section 4.5. We discuss the implications of our results for cosmic birefringence searches in Section 5 and conclude in Section 6.

2. DATA

2.1. Planck data

We use several publicly available data products produced by the Planck collaboration. The analysis in this work uses the recently released maps produced using the NPIPE processing pipeline (Planck Collaboration I 2020). We use observations taken with the Planck High Frequency Instrument (Planck Collaboration III 2020). We principally make use of the NPIPE 857, 353, and 217 GHz A/B data splits, which were independently ob-

served with different horns and are expected to have largely uncorrelated systematics. The NPIPE maps are all released in K_{CMB} temperature units, and the conversion factor to flux density units for the 857 GHz maps is $2.27 \text{ MJy sr}^{-1}/K_{\text{CMB}}$ (Planck Collaboration IX 2014; Planck Collaboration Int. LVII 2020). We further confirm our results using the Planck Data Release 3 (PR3) maps (Planck Collaboration I 2020), to ensure that our conclusions are not qualitatively affected by the choice of Planck processing pipeline.

2.2. HI-based Stokes parameter maps

Observations of HI are a valuable tool for deciphering the physical nature of dust emission. The column densities of HI and dust are linearly correlated in the diffuse ISM (Boulanger et al. 1996; Lenz et al. 2017), and thus the column density of HI is a useful proxy for the dust column. Recent work has shown a deeper link between these two tracers: the morphology of HI structure probes the polarization structure of the dust emission. Linear structures in diffuse HI emission are well aligned with the plane-of-sky magnetic field orientation traced by the dust polarization angle (Clark et al. 2015; Martin et al. 2015). The magnetic alignment is driven by density structures with properties consistent with the cold neutral medium phase of HI (McClure-Griffiths et al. 2006; Clark et al. 2019; Peek & Clark 2019; Kalberla & Haud 2020; Murray et al. 2020). Broadband measurements of dust polarization measure the line-of-sight integrated dust emission projected onto the plane of the sky, and thus changes in the polarization angle along the line of sight within a telescope beam contribute to depolarization of the measured dust signal. Clark (2018) showed that this line-of-sight magnetic field tangling can be predicted from the coherence of HI orientation as a function of HI velocity. Pelgrims et al. (2021) used this property of HI in conjunction with a Gaussian decomposition of HI data (Panopoulou & Lenz 2020) to detect line-of-sight frequency decorrelation in Planck data.

Clark & Hensley (2019) used these empirical relationships between HI and dust to construct three-dimensional (position-position-velocity) maps of the Stokes parameters of linear polarization predicted solely from the morphology of HI emission. These maps are integrated over line-of-sight velocity to produce Q_{HI} and U_{HI} , HI-based sky maps of the Stokes parameters of linear polarization. From these, the plane-of-sky magnetic field orientation inferred from the HI geometry is $\theta_{\text{HI}} = \frac{1}{2} \arctan \frac{U_{\text{HI}}}{Q_{\text{HI}}}$. Clark & Hensley (2019) compute two sets of maps using different HI surveys; in this analysis we use the $16.2'$ all-sky maps constructed from the HI4PI survey (HI4PI Collaboration et al. 2016). The Q_{HI} and

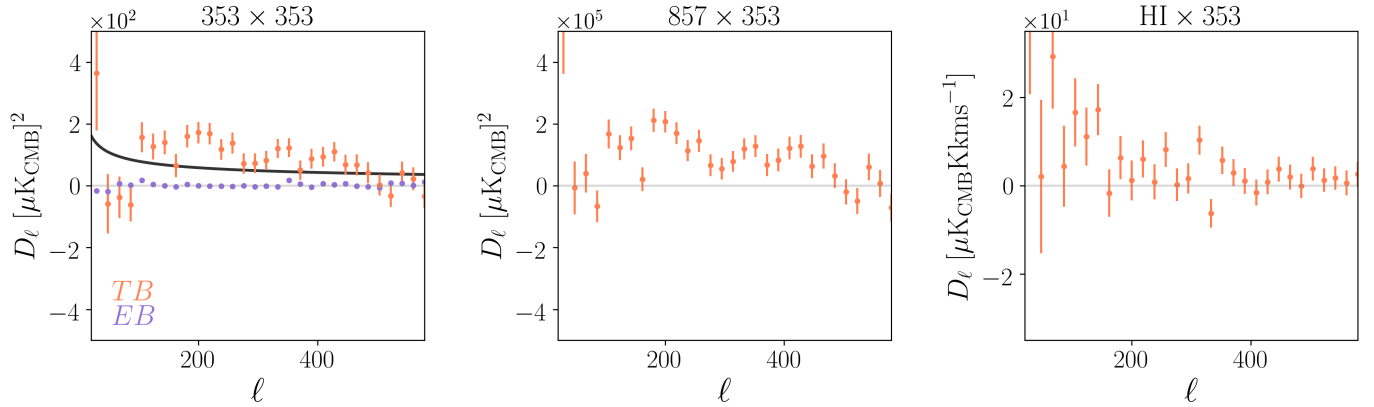


Figure 1. *TB* correlations (orange) computed with *T* total intensity maps, left to right: NPIPE 353 GHz (T_{353}), NPIPE 857 GHz (T_{857}), neutral hydrogen intensity (T_{HI}). B_{353} is computed from the NPIPE 353 GHz A/B splits. Leftmost panel also shows $E_{353}B_{353}$ computed from NPIPE A/B splits (purple). Black line in leftmost panel shows the fit to $T_{353}B_{353}$ calculated for PR3 data in Planck Collaboration XI (2020).

U_{HI} maps are integrated over $-90 < v_{\text{lsr}} < 90$ km/s. We also make use of T_{HI} , the HI total intensity over this same velocity range.

2.3. Sky masks

The primary results presented in this work are for cross-power spectra computed on the Planck 70% sky fraction Galactic plane mask (Planck Collaboration Int. XIX 2015). We apodize this mask with a $60'$ cosine taper such that our final mask has $f_{\text{sky}} = \frac{1}{N} \sum_i w_i^2 \sim 0.69$, where N is the number of map pixels and w_i is the fractional weight of each pixel.

The results demonstrating the origin of *TB* and *EB* in Galactic dust emission (e.g., Sections 4.2 and 4.3) are qualitatively unchanged for a simple sky mask defined by $|b| > 30^\circ$, and are similarly insensitive to the additional application of the Planck 353 GHz polarization point source mask (Planck Collaboration IX 2014). However, one of the important results of our work is that parity-odd quantities in dust polarization differ depending on the sky area considered. We note that our fiducial $f_{\text{sky}} \sim 0.69$ sky mask is very different from the sky masks considered in MK20. The ramifications of this difference are discussed in Section 5.

3. *TB*, OR NOT *TB*? EVIDENCE FOR A GLOBALLY NONZERO GALACTIC *TB* SIGNAL

We examine the *TB* signal over the high Galactic latitude sky, defined by the mask described in Section 2.3. The Planck *TB* analysis is based on the 353 GHz data for both total intensity and polarization (Planck Collaboration XI 2020). While 353 GHz is the Planck frequency channel most sensitive to dust emission in polarization, it is less sensitive than the 545 and 857 GHz channels to dust total intensity. We can thus compute the cross-

power spectra between a total intensity map at one frequency and the polarization maps at another, e.g., $T_{857}B_{353}$. We compute these cross-correlations from the NPIPE data splits described in Section 2. Whenever applicable, we compute the estimator for $T_{\nu_1}B_{\nu_2}$ as

$$T_{\nu_1}B_{\nu_2} = \frac{1}{2} (T_{\nu_1}^A B_{\nu_2}^B + T_{\nu_1}^B B_{\nu_2}^A), \quad (1)$$

where the *A* and *B* superscripts denote the two data splits (here assumed to have similar noise properties). We compute the analogous estimator for other quantities. We analyze $D_\ell = \ell(\ell+1)C_\ell/(2\pi)$, where C_ℓ is the pseudo- C_ℓ estimator for purified *E* and *B* modes (Smith 2006) computed with Namaster (Alonso et al. 2019). All results presented here are qualitatively insensitive to the choice of *E* and *B* purification. We estimate C_ℓ in bins of width $\Delta\ell = 19$. The error bars shown in Figure 1 represent Gaussian variance only, including contributions from both signal and noise. We also compute the correlation ratio

$$r_\ell^{XY} \equiv \frac{C_\ell^{XY}}{(C_\ell^{XX}C_\ell^{YY})^{1/2}}, \quad (2)$$

where *X* and *Y* are any of *T*, *E*, or *B*.

For $100 \lesssim \ell \lesssim 500$ we find a robustly positive $T_{353}B_{353}$ signal over our fiducial sky mask, with $\langle r_\ell^{TB} \rangle \sim 0.05$. The $T_{353}E_{353}$ signal is also robustly positive ($\langle r_\ell^{TE} \rangle \sim 0.23$ over the same multipole range). A spurious *TB* correlation could arise from the combination of the real *TE* signal and imperfect Planck polarization angle calibration (e.g., Abitbol et al. 2016). We estimate the polarization angle miscalibration required in order for the measured $T_{353}B_{353}$ to be entirely spurious, $TB^{\text{spurious}} = \sin(2\psi^{\text{miscal}})T_{353}E_{353}$ (e.g., Abitbol et al. 2016). We find that the Planck polarimeter mis-

calibration would need to be $\psi^{miscal} \sim 5^\circ$, strongly discrepant with the Planck polarization angle calibration uncertainty of 0.28° (Planck Collaboration Int. XLIX (2016), derived from pre-launch measurements described in Rosset et al. (2010)).

Weiland et al. (2020) report a significant nonzero TB signal for $T_{857}B_{353}$ and $T_{545}B_{353}$ computed with the PR3 data. We confirm that result using the NPIPE Planck maps (Figure 1). Weiland et al. (2020) also measure a nonzero $T_{\text{SFD}}B_{353}$ correlation, where T_{SFD} is a dust intensity map derived from IRAS and COBE data (Schlegel et al. 1998), and thus independent of Planck. This constitutes evidence that the nonzero TB is not an artifact of Planck systematics, except for the global polarization angle miscalibration discussed above. Weiland et al. (2020) further substitute B_{353} for B derived from either Wilkinson Microwave Anisotropy Probe (WMAP) K -band data (Page et al. 2007) or a template map described in Page et al. (2007) that is derived from optical starlight polarization data (Heiles 2000; Berdyugin et al. 2001, 2004; Berdyugin & Teerikorpi 2002). These measurements are independent of the Planck polarization angle calibration. The K -band data probe polarized synchrotron emission while the starlight is largely polarized by the same dust grains probed in the far infrared emission; either way, Weiland et al. (2020) find evidence for a positive TB correlation, and conclude that measurements of $TB > 0$ are real, rather than spurious.

As an additional test of the robustness of the TB correlation, we measure $T_{\text{HI}}B_{353}$, i.e., the cross-correlation between the HI4PI 21-cm total intensity and the Planck 353 GHz polarization. The HI data are entirely independent of the microwave data, and thus this calculation cannot be affected by correlated systematics between Planck frequency channels. As summarized in Figure 1, we measure a $T_{\text{HI}}B_{353}$ correlation that is consistent with positive TB , although the error bars are somewhat larger than the Planck-only measurements. Our results support the conclusion that nonzero TB is a real property of the Galactic emission.

4. THE ORIGIN OF PARITY VIOLATION IN DUST POLARIZATION

4.1. Hypothesis: Nonzero TB from magnetically misaligned dust filaments

We hypothesize that the observed nonzero TB_{353} is generated, at least in part, by filamentary ISM structures that are misaligned with the projected magnetic field in one preferential direction. A filament-induced TB correlation can be generated by a misalignment between the long filament axis and the plane-of-sky magnetic field orientation (Huffenberger et al. 2020). The

direction of misalignment determines the sign of TB , and thus if the statistical misalignment of filaments is skewed to one direction, the global signal will reflect that handedness.

Rather than E_{353} and B_{353} , we can consider E_{HI} and B_{HI} , derived from the HI-based Stokes parameter maps. These maps are constructed by measuring the orientation of filamentary HI structures: one of the underlying assumptions in the Clark & Hensley (2019) paradigm is that linear HI structure is preferentially parallel to the magnetic field. Filamentary ISM density structures that are aligned with the magnetic field generate a positive TE correlation (Zaldarriaga 2001; Huffenberger et al. 2020). We thus expect $T_{\text{HI}}E_{\text{HI}} > 0$ by construction. We do not have a reason to expect that $T_{\text{HI}}B_{\text{HI}}$ is robustly nonzero, as no coherent misalignment between the filament axis and θ_{HI} is included in the construction of the HI-based Stokes maps. This does not necessarily mean that θ_{HI} is perfectly aligned with the density structures in any of our T tracers: for one thing, the ISM contains a great deal of structure that is not well described as a linear filament with a single orientation. Also, the HI-based maps are the integration over the line of sight of 3D Stokes parameter maps constructed by quantifying the HI morphology in narrow HI velocity channels. Because of this line-of-sight integration, the θ_{HI} in a given pixel is an intensity-weighted average of the orientations of any HI structures along the line of sight (Clark 2018). Still, lacking an expectation of *coherent* misalignment between the HI intensity and the measured HI orientation, we expect $TB_{\text{HI}} \sim 0$.

We can demonstrate the misaligned filament effect by artificially introducing a global misalignment between θ_{HI} and the distribution of HI intensity. To do this, we globally rotate Q_{HI} and U_{HI} by some angle, and cross-correlate the rotated maps with T_{HI} , Q_{HI} , and U_{HI} . We apply this global rotation via

$$\begin{bmatrix} Q'_{\text{HI}} \\ U'_{\text{HI}} \end{bmatrix} = \begin{bmatrix} \cos(2\psi) & -\sin(2\psi) \\ \sin(2\psi) & \cos(2\psi) \end{bmatrix} \begin{bmatrix} Q_{\text{HI}} \\ U_{\text{HI}} \end{bmatrix}, \quad (3)$$

where ψ is the rotation angle applied to each pixel in the Q_{HI} and U_{HI} maps. We then compute E_{HI}' and B_{HI}' from Q_{HI}' and U_{HI}' , and show the resulting HI-based cross-correlations at $\ell = 140$ as a function of the rotation angle ψ in Figure 2. The choice of ℓ bin does not affect the shape or phase dependence of the signal; the ℓ bin affects only the relative amplitudes of TB , TE , and EB . The $\psi = 0$ values in Figure 2 represent the autocorrelation spectra of the raw (unrotated) Clark & Hensley (2019) maps. These maps display a strong, positive TE signal, and approximately zero TB and EB . When $\psi = 0$ the EE/BB ratio measured for these maps is also at

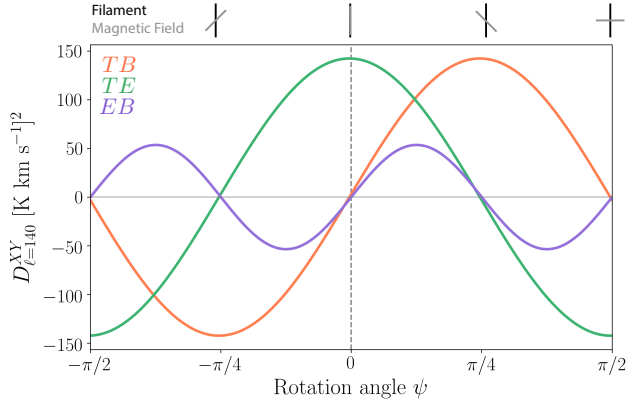


Figure 2. H_I×H_I cross-correlations as a function of a uniform rotation angle (ψ) applied to Q_{HI} and U_{HI} , described in Section 4.1. The cross-correlation amplitude is measured at $\ell = 140$ for the TB (orange), TE (green), and EB (purple) signals. Top axis illustrates the conceptual meaning of ψ . When $\psi = 0$, correlations are shown for the raw [Clark & Hensley \(2019\)](#) H_I-based Stokes parameter maps, for which filamentary H_I structures are perfectly aligned with the magnetic field by construction. Nonzero ψ represents a misalignment between H_I structures and the magnetic field, and the TB correlation peaks when $\psi = \pi/4$.

a maximum. This is consistent with our expectation that these H_I-based maps represent “perfect alignment” between density structures and the magnetic field by construction.

The introduction of nonzero ψ represents an artificial, uniform misalignment between the H_I structures and the magnetic field. When $\psi = 0$, $T_{\text{HI}}B_{\text{HI}}'$ is consistent with 0, and $T_{\text{HI}}E_{\text{HI}}'$ is at its maximum value. $T_{\text{HI}}B_{\text{HI}}'$ is at a maximum when $\psi = \pi/4$ and at a minimum when $\psi = -\pi/4$. This is consistent with our intuitive expectation that a 45° misalignment between a filament and the magnetic field will generate the strongest B -mode polarization signal.

This calculation also clearly demonstrates that if filament misalignment is generating nonzero TB , it necessarily also generates nonzero EB (except for $\psi = \pm\pi/4$, but this would yield zero TE). Furthermore, in this simplified misaligned filament model, the sign and magnitude of EB can be predicted by measuring TE and TB . This carries important implications that we will return to in Section 5. Here, we will test whether there is evidence for a misaligned filament origin for the nonzero TB_{353} in Planck data.

4.2. TB is related to $\Delta\theta(\text{HI}, 353)$

We introduce a proxy for the degree of local filament misalignment by quantifying the difference between the

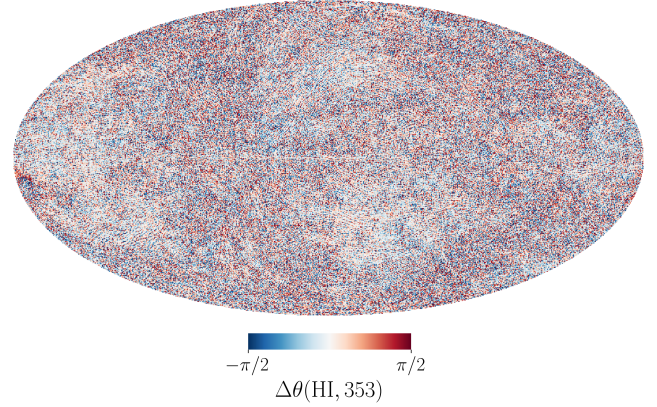


Figure 3. Map of $\Delta\theta(\text{HI}, 353)$, the signed angular difference between Planck θ_{353} and θ_{HI} computed from the [Clark & Hensley \(2019\)](#) maps. $\Delta\theta(\text{HI}, 353)$ is calculated at 16.2' resolution, the native resolution of H_I4PI. This map is in a mollweide projection centered at $(l, b) = (0, 0)$.

353 GHz polarization angle and the H_I-based polarization angle. We define

$$\Delta\theta(1, 2) = \frac{1}{2} \arctan \left(\frac{\sin(2\theta_1) \cos(2\theta_2) - \cos(2\theta_1) \sin(2\theta_2)}{\cos(2\theta_1) \cos(2\theta_2) + \sin(2\theta_1) \sin(2\theta_2)} \right), \quad (4)$$

the signed difference between angles θ_1 and θ_2 . We apply Equation 4 to θ_{HI} and θ_{353} calculated from the NPIPE full maps to compute $\Delta\theta(\text{HI}, 353)$, the signed angular difference between the H_I-based polarization angle and the 353 GHz polarization angle. We compute $\Delta\theta(\text{HI}, 353)$ at the 16.2' resolution of the H_I4PI data (Figure 3).

If the observed nonzero TB is related to a misalignment between ISM density structures and the magnetic field, the observed TB signal should be related to $\Delta\theta(\text{HI}, 353)$, our proxy for the angular difference between the orientation of dusty filaments and the local magnetic field. In particular, we expect the sign of $\Delta\theta(\text{HI}, 353)$ to be correlated with the sign of TB .

We test a series of modifications to the Planck 353 GHz polarization data to test the hypothesis that the Galactic TB signal is related to $\Delta\theta(\text{HI}, 353)$. For each test we modify Q_{353} and U_{353} by applying a rotation by an angle ψ to each pixel based on some criterion. We compute

$$\begin{bmatrix} Q'_{353} \\ U'_{353} \end{bmatrix} = \begin{bmatrix} \cos(2\psi) & -\sin(2\psi) \\ \sin(2\psi) & \cos(2\psi) \end{bmatrix} \begin{bmatrix} Q_{353} \\ U_{353} \end{bmatrix} \quad (5)$$

where ψ is determined based on the sign of $\Delta\theta(\text{HI}, 353)$, i.e., ψ is one of

$$\psi^+ = \begin{cases} \mathcal{R}, & \text{if } \Delta\theta(\text{HI}, 353) > 0 \\ 0, & \text{otherwise} \end{cases} \quad (6)$$

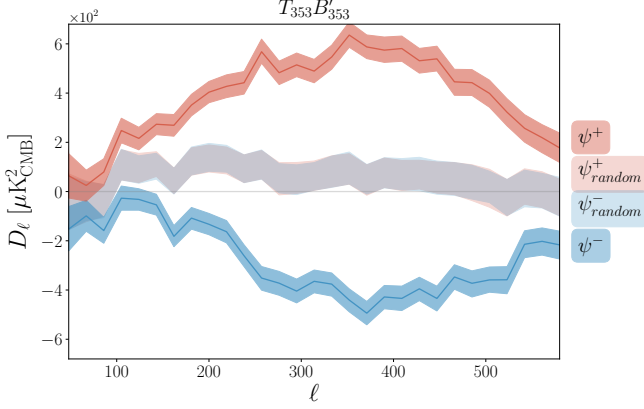


Figure 4. $T_{353}B'_{353}$, cross-correlation of the NPIPE 353 GHz total intensity and polarization data for the experiment described in Section 4.2. Red: median (line) and 1σ spread (contours) of 100 realizations of $T_{353}B'_{353} \pm \sigma_{TB'}$ after rotating the 353 GHz polarization angles of pixels with $\Delta\theta(\text{HI}, 353) > 0$ by a random angle (ψ^+ , Equation 6). Blue: analogous calculation with random rotation applied to pixels with $\Delta\theta(\text{HI}, 353) < 0$ (ψ^- , Equation 7). Lighter contours show null tests (light red: Equation 8, light blue: Equation 9). $T_{353}B'_{353}$ becomes strongly negative or positive when the 353 GHz polarization angles are randomized based on the sign of $\Delta\theta(\text{HI}, 353)$.

or

$$\psi^- = \begin{cases} \mathcal{R}, & \text{if } \Delta\theta(\text{HI}, 353) < 0 \\ 0, & \text{otherwise} \end{cases} \quad (7)$$

where \mathcal{R} is a random variable drawn uniformly from the interval $[-\pi/2, \pi/2]$. The rotation of Q_{353} and U_{353} by a random number preserves the 353 GHz polarized intensity in each pixel, while randomizing the polarization angle. Applying Equation 5 with $\psi = \psi^+$ is equivalent to rotating the 353 GHz polarization angle by a random value in all pixels with positive $\Delta\theta(\text{HI}, 353)$, and otherwise leaving the pixels unchanged.

This formalism allows us to test the influence of the polarization angle structure of pixels with a given sign of $\Delta\theta(\text{HI}, 353)$ on the global $T_{353}B'_{353}$ signal. To interpret the results, we also need a null test. We generate 100 map realizations of Δ_{syn} , a Gaussian random field with the same power spectrum as $\Delta\theta(\text{HI}, 353)$, and apply Equation 5 to each map with ψ determined by

$$\psi^+_{random} = \begin{cases} \mathcal{R}, & \text{if } \Delta_{syn} > 0 \\ 0, & \text{otherwise} \end{cases} \quad (8)$$

or

$$\psi^-_{random} = \begin{cases} \mathcal{R}, & \text{if } \Delta_{syn} < 0 \\ 0, & \text{otherwise.} \end{cases} \quad (9)$$

For each of these maps we compute $T_{353}B'_{353}$. The results are shown in Figure 4. The null tests, i.e., randomizing the 353 GHz polarization angles for pixels selected based on the sign of Δ_{syn} , produce $T_{353}B'_{353}$ correlations that are \lesssim the unrotated $T_{353}B_{353}$: either consistent with 0 or weakly positive. By contrast, randomizing the 353 GHz polarization angle for pixels with $\Delta\theta(\text{HI}, 353) > 0$ produces a strong positive $T_{353}B'_{353}$ signal. Randomizing the polarization angle of pixels with $\Delta\theta(\text{HI}, 353) < 0$ produces a strongly negative $T_{353}B'_{353}$ signal. Evidently, the sign of $\Delta\theta(\text{HI}, 353)$ is predictive of the sign of the Planck TB signal.

One interpretation of these experiments is that by randomizing the polarization angle, we “destroy” the correlations that exist between the total intensity and polarization angle for approximately half of the sky in each test. If there were no correlation between the pixel selection map and the sign of TB , this process should only introduce noise to the map, and we should not expect to strengthen the magnitude of TB . This is consistent with what we find when we randomize polarization angles based on the sign of Δ_{syn} . Likewise, rotating *all* 353 GHz polarization angles by \mathcal{R} results in $T_{353}B'_{353} \sim 0$, as expected. By contrast, when we randomize polarization angles based on the sign of $\Delta\theta(\text{HI}, 353)$, we seem to preferentially add noise to regions of the sky that give rise to one sign of TB . The strong positive $T_{353}B'_{353}$ correlation that we find when we randomize the polarization angles of pixels with $\Delta\theta(\text{HI}, 353) > 0$ is consistent with the hypothesis that pixels with $\Delta\theta(\text{HI}, 353) > 0$ are preferentially in regions of sky with a negative $T_{353}B_{353}$. Likewise, this suggests that pixels with $\Delta\theta(\text{HI}, 353) < 0$ are preferentially in regions of sky with positive $T_{353}B_{353}$. Note that which sign of $\Delta\theta(\text{HI}, 353)$ is associated with a given sign of TB depends on the particular conventions used (n.b. $\Delta\theta(\text{HI}, 353) = -\Delta\theta(353, \text{HI})$), but the association of the sign of $\Delta\theta(\text{HI}, 353)$ with the sign of TB is robust.

We consider a number of variations of this experiment and find that they are all consistent with the same hypothesis. We find qualitatively the same result if we replace \mathcal{R} in Equations 6 – 9 with $\Delta\theta(\text{HI}, 353)$, so that rather than rotating by a random angle, we rotate the polarization angles of selected pixels by $\Delta\theta(\text{HI}, 353)$. In this variant, $T_{353}B'_{353}$ is nonzero at a higher significance for the maps constructed with ψ^+ and ψ^- than for maps constructed with ψ^+_{random} and ψ^-_{random} . We also test a different framework: instead of applying Equation 5, we scramble (resample without replacement) Q_{353} and U_{353} over sets of pixels defined either by the sign of $\Delta\theta(\text{HI}, 353)$ or by the sign of Δ_{syn} . This approach changes the sky distribution of the 353 GHz polarized

intensity. Nevertheless, we still find that pixel resampling based on the sign of $\Delta\theta(\text{HI}, 353)$ strengthens the magnitude of the $T_{353}B'_{353}$ signal more than resampling based on the sign of Δ_{syn} , albeit at lower significance than the rotation-based method that preserves the polarized intensity. We find the same behavior for $T_{353}B'_{353}$ and $T_{217}B'_{217}$. If we construct $\Delta\theta(\text{HI}, 353)$ from maps of Q_{HI} , U_{HI} , Q_{353} , and U_{353} smoothed to a uniform resolution of FWHM=30', 50', or 80' and perform the same experiment (without downgrading the pixelization of the maps), we measure the same discrimination between positive and negative TB based on the sign of $\Delta\theta(\text{HI}, 353)$, with the largest magnitude of the effect pushed to increasingly lower multipoles as the angular resolution of $\Delta\theta(\text{HI}, 353)$ is lowered.

Could these results be explained by some latent correlation between $\Delta\theta(\text{HI}, 353)$ and the 353 GHz polarization angles that is not physically related to a misalignment between HI structures and the magnetic field? The magnitude of $|\Delta\theta(\text{HI}, 353)|$, for instance, is anti-correlated with the local polarization angle dispersion (see Figure 12 in Clark & Hensley 2019). Physically, this is consistent with the expectation that the dispersion of polarization angles is higher when the mean magnetic field is more parallel to the line of sight (e.g., Hensley et al. 2019). This 3D geometry affects the magnitude of $\Delta\theta(\text{HI}, 353)$, but does not on its own introduce a preference for the sign of $\Delta\theta(\text{HI}, 353)$. We find no evidence for a correlation between the sign of $\Delta\theta(\text{HI}, 353)$ and the numerical value of θ_{353} .

The results shown in Figure 4 are qualitatively unchanged for $\Delta\theta(\text{HI}, 353)$ derived from Planck PR3 or NPIPE maps. Deriving $\Delta\theta(\text{HI}, 353)$ from alternative θ_{HI} maps based on the spatial gradient of HI4PI channel map emission (Clark & Hensley 2019) also yields qualitatively similar results. We likewise reproduce the same qualitative results when we calculate $T_{353}B'_{353}$ using the PR3 maps. We conclude that the association between the sign of $\Delta\theta(\text{HI}, 353)$ and the sign of TB is not an artifact of any known systematic in the processing of Planck data, nor in the calculation of θ_{HI} .

The framework presented here allows us to test hypotheses for the physical nature of TB , or any other statistical measure, by randomizing some polarization angles based on test criteria. The conditions on $\Delta\theta(\text{HI}, 353)$ in Equations 6 and 7 enable a test of the hypothesis that the sign of $\Delta\theta(\text{HI}, 353)$ is related to the sign of TB . The most general expression of our formalism is the application of Equation 5 with $\psi = \psi_{\text{condition}}$, where

$$\psi_{\text{condition}} = \begin{cases} \mathcal{R}, & \text{if [condition]} \\ 0, & \text{otherwise.} \end{cases} \quad (10)$$

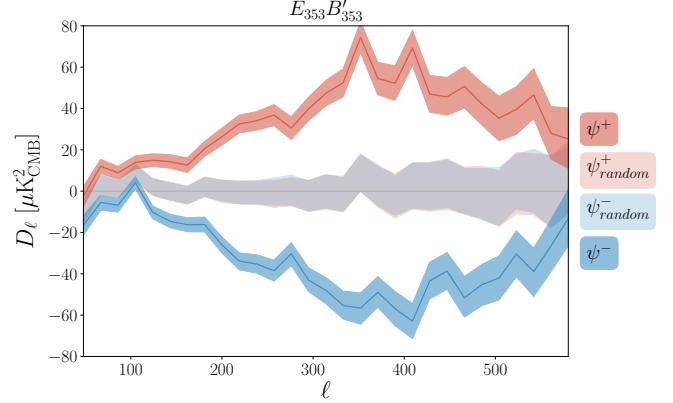


Figure 5. The same experiment depicted in Figure 4, but for the EB correlation at 353 GHz (Section 4.3). The cross-correlated maps are the NPIPE A/B splits of the 353 GHz data. Red and blue contours show the 1σ distribution of 100 realizations of $E_{353}B'_{353} \pm \sigma_{EB'}$ when the polarization angles of the data used to compute B'_{353} are randomized if $\Delta\theta(\text{HI}, 353) > 0$ (red) or $\Delta\theta(\text{HI}, 353) < 0$ (blue). Light blue and red contours show the 1σ distribution of the null tests (Equations 8 and 9).

We test the additional hypothesis that the sign of TB is related to N_{HI} , the HI column density, by applying Equation 10 with conditions on N_{HI} , e.g., $N_{\text{HI}} > \text{med}(N_{\text{HI}})$ or $P_i(N_{\text{HI}}) < N_{\text{HI}} < P_{i+10}(N_{\text{HI}})$, where P_i is the i^{th} percentile of N_{HI} . We find no strong evidence for a correlation between N_{HI} and the sign of TB .

4.3. EB is related to $\Delta\theta(\text{HI}, 353)$

If the relative orientation of the magnetic field and dusty filaments is responsible for generating nonzero Galactic TE and TB , it follows that these filaments will also generate nonzero EB . The relative amplitude of TB , TE , and EB as a function of misalignment angle is illustrated in Figure 2. The sign of EB is uniquely determined by the combined signs of TB and TE in the misaligned filament paradigm. Because TE is robustly positive over the sky, it follows that EB in this model will have the same sign as TB . TB , in turn, may change sign depending on the sky mask and angular scale considered, and it follows that the sign of the Galactic EB signal will be mask-dependent as well.

We test whether there is evidence in the Planck data for an EB signal associated with $\Delta\theta(\text{HI}, 353)$. We apply the same experiment described in Section 4.2, but measure the estimator for the $E_{353}B'_{353}$ cross-correlation between A and B splits of the NPIPE 353 GHz data, where we apply the angle rotation to the data split used to calculate B_{353} . The results are shown in Figure 5. We find that randomly rotating the polarization angles of pixels based on the sign of $\Delta\theta(\text{HI}, 353)$ yields

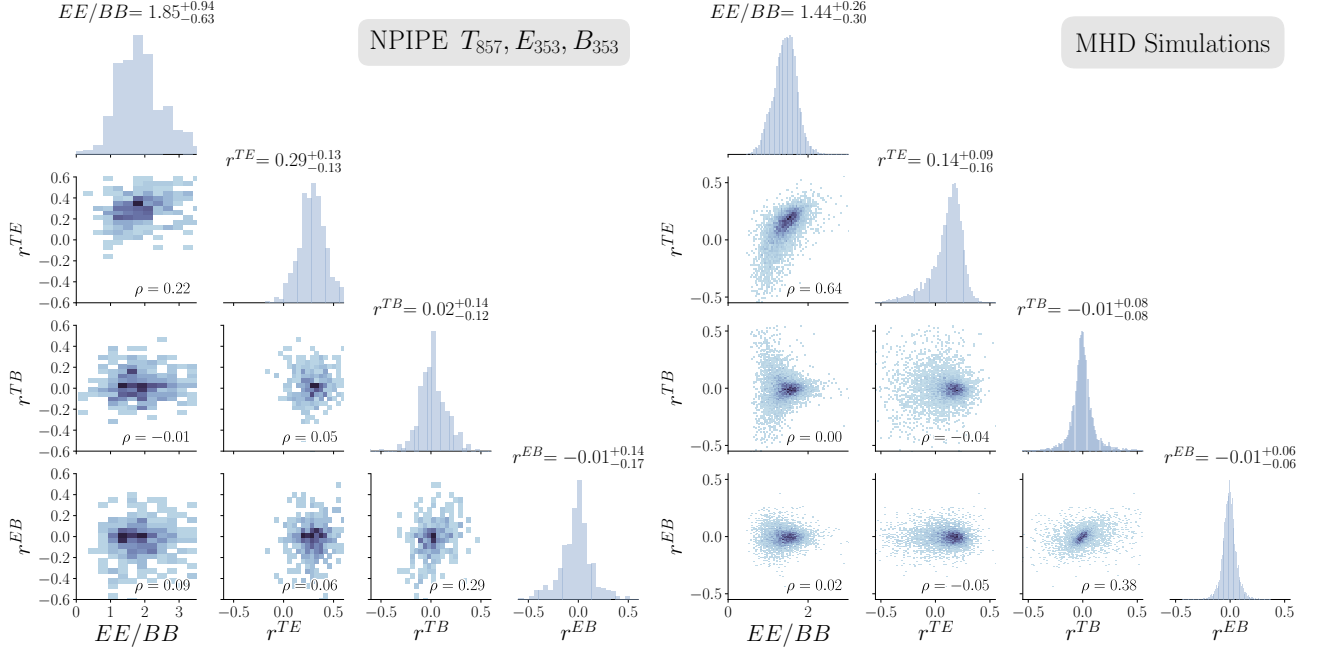


Figure 6. Joint distributions between EE/BB and normalized cross-correlations r^{TE} , r^{TB} , and r^{EB} , computed at $\ell = 200$. Left: Correlations between NPIPE T_{857} , E_{353} , and B_{353} data computed for 12° radius circular regions of data with $|b| > 30^\circ$. Right: Correlations between 3150 synthetic maps from Kim et al. (2019). For each map we compute two sets of correlations, for $b > 30^\circ$ and $b < -30^\circ$. The Spearman’s rank correlation coefficient of each joint distribution is shown in the bottom-right corner of each panel. Diagonal plots show the 1D histograms of each quantity, labeled with the median, 16th, and 84th percentile values.

nonzero $E_{353}B'_{353}$ in excess of associated null tests. As with our TB experiment, applying Equation 6 to the 353 GHz data generates positive $E_{353}B'_{353}$ over the ℓ range where the $\Delta\theta(\text{HI}, 353)$ -selected data are distinguishable from the null tests, and applying Equation 7 yields negative $E_{353}B'_{353}$. We find the same behavior for $E_{217}B'_{217}$. We conclude that the sign of EB is related to the sign of $\Delta\theta(\text{HI}, 353)$, and that the sign of EB relative to $\Delta\theta(\text{HI}, 353)$ has the same sense as the sign of TB .

4.4. Interpretation: Nonzero TB and EB from magnetically misaligned filaments

The results in Sections 4.2 and 4.3 indicate that the magnetic misalignment probed by $\Delta\theta(\text{HI}, 353)$ is correlated with the TB and EB signals in polarized dust emission. As we predicted, the sign of $\Delta\theta(\text{HI}, 353)$ probes the “handedness” of the local magnetic misalignment of filaments. The globally positive TB signal (Figure 1) thus suggests that there is an overall preference for one handedness of the misalignment over our fiducial sky mask. In our convention, randomizing the polarization angles of pixels with positive $\Delta\theta(\text{HI}, 353)$ leads to a positive global TB : this suggests that the handedness associated with negative $\Delta\theta(\text{HI}, 353)$ is associated with positive TB . Put another way, the globally positive TB suggests that there exists a slight preference for ISM density structures within our

sky area to be misaligned with $-\pi/2 < \Delta\theta(\text{HI}, 353) < 0$ in our convention. It is possible that there is no physical preference for this handedness in the ISM, and that $TB > 0$ is simply the realization of the projected sky that we happen to observe. Alternatively, there may be a true physical preference for this handedness encoded in the formation of dusty filaments.

$\Delta\theta(\text{HI}, 353)$ measures the degree of alignment between the intensity structure traced by HI and the plane-of-sky magnetic field inferred from the 353 GHz dust polarization angle. If the line-of-sight-averaged dust polarization angle traces the integrated, sky-projected magnetic field orientation as is commonly assumed, nonzero $\Delta\theta(\text{HI}, 353)$ indicates that the HI structures are misaligned with the plane-of-sky magnetic field. However, if there exists a coherent misalignment between dust grains and the local magnetic field, the HI structures could be perfectly aligned with the magnetic field, and we would still measure nonzero $\Delta\theta(\text{HI}, 353)$. $\Delta\theta(\text{HI}, 353)$ in that case would correspond to the relative orientation of the magnetic field and the alignment direction of interstellar grains. Such discrepancies can arise in the presence of radiative torques from an anisotropic radiation field (Draine & Weingartner 1997). In the next section, however, we test predictions of our model using MHD simulations that do not model grain

alignment and yet agree with our predictions. Thus, grain alignment along a direction other than the local magnetic field is a possible but likely subdominant contributor to the Galactic TB signal.

4.5. Tests of correlation predictions with data and MHD simulations

Sections 4.2 and 4.3 demonstrate that $\Delta\theta(\text{HI}, 353)$ is predictive of the signs of both TB and EB . Because $\Delta\theta(\text{HI}, 353)$ varies across the sky (Figure 3), this result implies that the global TB and EB signals are mask-dependent quantities. Our results imply that in principle, it is possible to identify regions of sky for which the dust TB and EB are negative. In practice, it may be difficult to define sky masks capable of isolating negative TB in Planck data, given the non-trivial spatial structure in $\Delta\theta(\text{HI}, 353)$.

From the magnetically misaligned filament picture we also make predictions for the relative amplitudes of TB , TE , and EB . In particular, if TE is strong and positive ($\psi \sim 0$ in Figure 2), small deviations from perfect alignment between dust filaments and the local magnetic field will generate a correlation between TB and EB . Conversely, if TE is strong and *negative* ($\psi \sim \pm\pi/2$), small deviations from perfect anti-alignment between dust filaments and the local magnetic field will lead to an *anti*-correlation between TB and EB . In addition, in the regime where TB is strong and positive ($\psi \sim \pi/4$) or negative ($\psi \sim -\pi/4$), TE and EB should be correlated or anti-correlated, respectively.

To investigate these correlations in Planck data, we tile the sky with 12° radius circular regions centered on $N_{\text{side}}=8$ HealPix pixels (Górski et al. 2005), additionally applying our fiducial mask, and apodize each region with a 2° cosine taper (similar to analyses in Planck Collaboration Int. XXX 2016; Krachmalnicoff et al. 2018; Bracco et al. 2019b). We compute cross-correlations between T_{857} , E_{353} , and B_{353} , using splits of the NPIPE data as in the preceding analysis. The lefthand panel of Figure 6 shows the joint distribution between r^{TE} , r^{TB} , r^{EB} , and $EE/BB \equiv C_\ell^{EE}/C_\ell^{BB}$, where T is T_{857} and E, B are E_{353}, B_{353} . These values are computed for a multipole bin of width $\Delta\ell = 200$ centered at $\ell = 200$. The TE correlation is generally strongly positive over the sky regions considered. We find weak positive correlations between EE/BB and r^{TE} (Spearman’s rank coefficient $\rho \sim 0.2$) and between r^{TB} and r^{EB} ($\rho \sim 0.3$). The results are similar when we use T_{353} instead.

The Planck data are thus consistent with the behavior we predict when filaments are on average well-aligned with the magnetic field. However, we are limited in our ability to fully test the predicted correlations in data

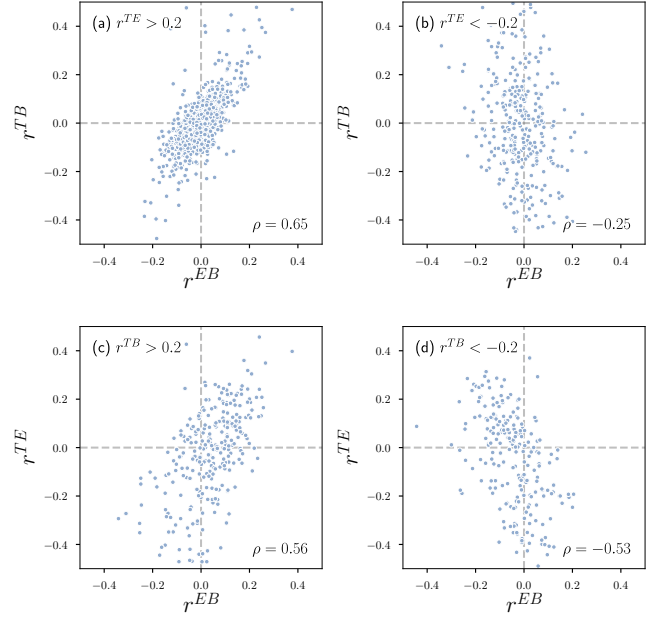


Figure 7. Joint distributions of normalized correlations in selected synthetic maps for (a) strong, positive TE ($r^{TE} > 0.2$), (b) strong, negative TE ($r^{TE} < -0.2$), (c) strong, positive TB ($r^{TB} > 0.2$), and (d) strong, negative TB ($r^{TB} < -0.2$). Each selection produces the expected correlations as quantified by the Spearman’s rank correlation coefficient presented in the bottom-right corner of each panel.

because the sky, even analyzed in small regions, is in the regime where the TE signal is strong and positive ($\psi \sim 0$). To further test our predictions, we use synthetic dust polarization maps presented in Kim et al. (2019). The maps are derived from MHD simulations based on a solar neighborhood model that includes self-gravity, Galactic differential rotation, cooling and heating, and star formation and supernova feedback (Kim & Ostriker 2017). A total of 3150 maps with $N_{\text{side}}=128$ are publicly available.² For each map we apply a simple hemispheric mask, defined by either $b > 30^\circ$ or $b < -30^\circ$, and compute the pseudo- C_ℓ for purified E - and B -modes using Namaster, as in our analysis of the Planck data. We note that the limited resolution of numerical simulations steepens the power spectra at turbulence dissipation scales (typically $\sim 10 - 20$ pixels). The projection of cubic resolution elements onto a Healpix sky as viewed by an observer placed within the simulation domain gives rise to non-trivial projection effects, preventing a clear separation of the inertial range and dissipation scales and further steepening the power spectral slopes for the synthetic maps. However, the cor-

² https://lambda.gsfc.nasa.gov/simulation/tb_tigress_data.cfm

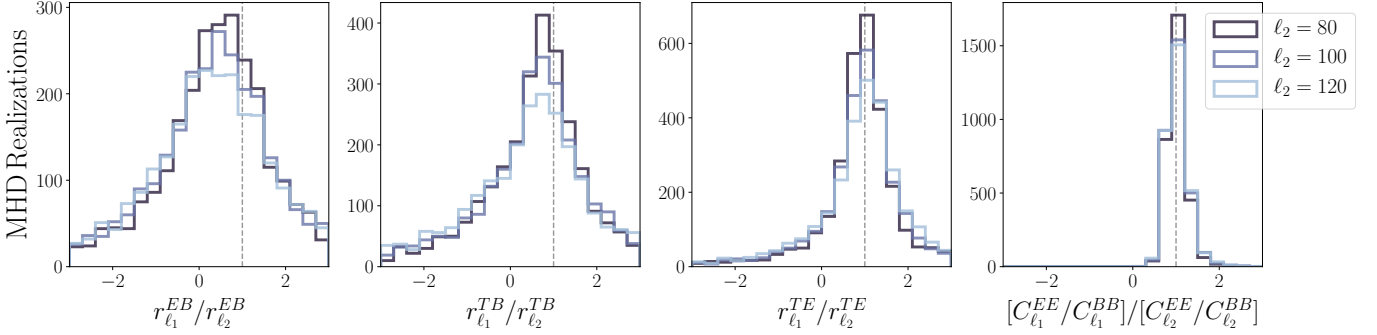


Figure 8. Histograms of the ratio of two ℓ bins over 3150 realizations of the MHD simulations. Bin ratios are computed for r^{EB} , r^{TB} , r^{TE} , EE/BB , from left to right. Each histogram plots the ratio of $\ell_1 = 60$ to $\ell_2 = 80, 100$, or 120 .

relation ratios we measure are robust to these effects, and are converged with different resolutions (Kim et al. 2019).

The righthand panel of Figure 6 shows the joint distributions for r^{XY} and EE/BB computed from the simulated maps. The majority of the synthetic maps show $EE/BB > 1$ and $r^{TE} > 0$, and we find a positive correlation between EE/BB and r^{TE} ($\rho = 0.64$). There is also a weak positive correlation between r^{TB} and r^{EB} ($\rho = 0.38$). This positive correlation is consistent with the prediction illustrated by Figure 2, as the synthetic maps are dominated by strong, positive TE signals. The TB and EB signals are on average zero. There are no significant correlations among the other quantities. These correlations are qualitatively consistent with the Planck data.

We further test our predictions by selecting realizations of the sky that demonstrate strong TE or TB of a given sign. Figure 7 shows correlations for synthetic maps with (a) strong, positive TE ($r^{TE} > 0.2$), (b) strong, negative TE ($r^{TE} < -0.2$), (c) strong, positive TB ($r^{TB} > 0.2$), and (d) strong, negative TB ($r^{TB} < -0.2$). Of our 6300 sets of power spectra (North and South hemispheres for 3150 synthetic maps), we find that these criteria are satisfied for (a) 1629, (b) 315, (c) 282, and (d) 232 maps. We confirm our predictions in all regimes. Selecting maps with strong, positive TE significantly enhances the correlation between TB and EB seen in Figure 6 ($\rho = 0.38 \rightarrow 0.65$). The maps with strong, negative TE show the predicted anti-correlation between TE and EB ($\rho = -0.25$). Finally, while the full suite of simulations shows no correlation between r^{TE} and r^{EB} ($\rho = -0.05$, Figure 6), the predicted correlations appear when we select maps based on their TB correlations. Selecting maps with strong positive TB yields the predicted positive correlation between EB and TE (Figure 7 panel c, $\rho = 0.56$); selecting maps with strong negative TB yields a negative correlation between EB and TE (panel d, $\rho = -0.53$). In all cases we show the

same $\ell = 200$ bin that we use to compute correlations in the Planck data. We also compute these correlations for a bin of width $\Delta\ell = 40$ centered at $\ell = 80$. The measured correlations are comparable or stronger at lower multipole, and still in agreement with predictions: at $\ell = 80$ we find (a) $\rho = 0.65$, (b) $\rho = -0.41$, (c) $\rho = 0.64$, and (d) $\rho = -0.58$.

In the polarized filament picture, the EE/BB ratio should have some dependence on how well aligned filaments are with the local magnetic field, irrespective of the handedness of any misalignment. Filaments that are well-aligned either parallel or perpendicular to the magnetic field should generate strong E -like polarized emission, and thus tend to have higher EE/BB ratios. Filaments with a misalignment angle $\psi \sim \pm\pi/4$ should have strong B -like emission, and therefore lower EE/BB . We therefore expect that in general, EE/BB will be positively correlated with $|r^{TE}|$, the absolute magnitude of the TE correlation ratio. Likewise, EE/BB should be negatively correlated with $|r^{TB}|$. Both of these expectations are borne out in the MHD simulations ($\rho = 0.38, \rho = -0.44$, respectively, for the realizations shown in Figure 6). However, the EE/BB ratio is also sensitive to effects other than the degree of magnetic alignment. The strength of EE/BB also depends on the aspect ratios of polarized dust filaments: filaments that are longer relative to their widths will tend to have higher EE/BB (Rotti & Huppenberger 2019). Furthermore, polarized emission in both the real sky and the MHD simulations does not solely originate from filamentary structures. It may be the case that filaments contribute a larger proportion of the TE , TB , and EB amplitudes than the EE and BB amplitudes.

We investigate the scale dependence of r_ℓ^{EB} , r_ℓ^{TB} , r_ℓ^{TE} , and EE/BB in the simulations by computing ratios of each of these quantities between two ℓ bins (Figure 8). For this calculation we use the same 3150 maps, but compute cross-correlations over a single $|b| > 30^\circ$ mask for each map, using a fixed bin width of $\Delta\ell = 10$.

Figure 8 shows the ratio of $\ell_1 = 60$ to $\ell_2 = 80$, 100, or 120 for each of these quantities. We find that the EE/BB ratio is nearly scale-independent over this multipole range, with a histogram sharply peaked at $[EE_{\ell_1}/BB_{\ell_1}]/[EE_{\ell_2}/BB_{\ell_2}] = 1$. By contrast, we find that the synthetic r^{TE} , r^{TB} , and r^{EB} data are less constant in ℓ , although $r_{\ell_1}^{TE}/r_{\ell_2}^{TE}$ in particular is still strongly peaked at unity. Planck constraints do not find strong evidence for an ℓ -dependent TE correlation around these angular scales (Planck Collaboration XI 2020). As discussed above, the correlation ratios considered here are generally robust to resolution and projection effects. The ℓ bins used for the calculation shown in Figure 8 represent the range over which the resolution convergence is demonstrated in Kim et al. (2019).

In principle, it may be possible to identify small regions of the sky with negative TE , where these correlations could be further tested in real data. Observations of polarized dust emission show evidence that the relative orientation of density structures with respect to the plane-of-sky magnetic field changes from preferentially parallel to more perpendicular at higher column densities (Planck Collaboration Int. XXXII 2016; Planck Collaboration Int. XXXV 2016; Soler et al. 2017; Jow et al. 2018). A magnetic field oriented orthogonally to the main axis of a filament would produce polarized emission with a negative TE correlation (Zaldarriaga 2001; Huffenberger et al. 2020). It is thus reasonable to expect that high column density regions of sky might have negative TE (Bracco et al. 2019b). This could be tested in measurements of dust emission at higher angular resolution, with \sim arcminute-resolution dust polarization maps made by ground-based CMB experiments like the Atacama Cosmology Telescope (Aiola et al. 2020; Naess et al. 2020) and the South Pole Telescope (Benson et al. 2014), as well as next-generation or proposed experiments like the Simons Observatory (Ade et al. 2019), CMB-S4 (Abazajian et al. 2016, 2019), CCAT-prime (Choi et al. 2020a), and PICO (Hanany et al. 2019).

5. IMPLICATIONS FOR COSMIC BIREFRINGENCE ANALYSES

MK20 found evidence for a nonzero isotropic cosmic birefringence angle at 2.4σ significance using Planck PR3 data, assuming that the foreground Galactic EB signal vanishes. Our results imply that the Galactic EB signal is generally nonzero, and that the sign of EB can be predicted from the signs of TE and TB measured using the same sky mask. For our fiducial mask, we measure robustly positive TE and TB in Planck NPIPE data over $100 \lesssim \ell \lesssim 500$, and thus expect a positive EB

contribution from dust. We caution that a different sky mask can yield a different result.

In addition to the sign of the Galactic EB signal, we can estimate its amplitude. Given a measurement of TB and TE in the polarized dust emission, we estimate the global magnetic misalignment angle consistent with these measurements as

$$\psi_\ell^{dust} = \frac{1}{2} \arctan \frac{C_\ell^{TB}}{C_\ell^{TE}}. \quad (11)$$

If we were able to isolate the TE and TB emission from a single filament on the sky, the form of this equation would parameterize the angle between the filament long axis and the local magnetic field orientation (i.e., the quantity for which $\Delta\theta(\text{HI}, 353)$ is our proxy). This form also parameterizes a global magnetic misalignment angle, as illustrated in Figure 2. By computing ψ_ℓ^{dust} as a single ℓ -dependent quantity over our sky mask, we are parameterizing a scale-dependent “effective magnetic misalignment” over the sky area considered. This measurement represents the net misalignment angle from the contributions of many dusty filaments, not only the “one-filament term” (considered by Huffenberger et al. (2020), in analogy to the one-halo term in galaxy formation theory). We estimate ψ_ℓ^{dust} using the NPIPE data splits over our fiducial mask and find $\psi_\ell^{dust} \sim 5^\circ$ for $100 \lesssim \ell \lesssim 500$ (Figure 9, lefthand panel).

From ψ_ℓ^{dust} , the predicted sign of the dust C_ℓ^{EB} is immediately apparent (e.g., Figure 2). We could estimate the amplitude of the dust EB by treating ψ_ℓ^{dust} as a global miscalibration angle, such that the amplitude of EB would be proportional to $EE - BB$ (e.g., Abitbol et al. 2016; Minami et al. 2019). However, we expect that this treatment will generally overestimate the dust EB , because the observed EE and BB contain signal from both filamentary structures, which should contribute substantially to EB , and the rest of the dust, which we do not expect to contribute strongly to EB . We instead adopt $r_\ell^{EB} \leq r_\ell^{TB}$, and estimate

$$r_\ell^{EB, dust} = r_\ell^{TB} \sin(4\psi_\ell^{dust}) \quad (12)$$

as an upper limit on the expected EB correlation ratio.

From Equation 12 and our measurement of r_ℓ^{TB} at 353 GHz, we estimate $\langle r_\ell^{EB} \rangle \sim 0.017$, where the average is computed on the binned r_ℓ^{EB} over $100 \lesssim \ell \lesssim 500$. Considering our measurements of EE and BB , this translates to an amplitude $\langle D_\ell^{EB} \rangle \lesssim 2.5 \mu\text{K}_{\text{CMB}}^2$ at 353 GHz. This is of the same order as the statistical uncertainty on EB in Planck data, although measurements of EB in the 353 GHz data over our mask are largely consistent with our (signed) upper limit prediction. Measuring this intrinsic dust EB should be a target of future

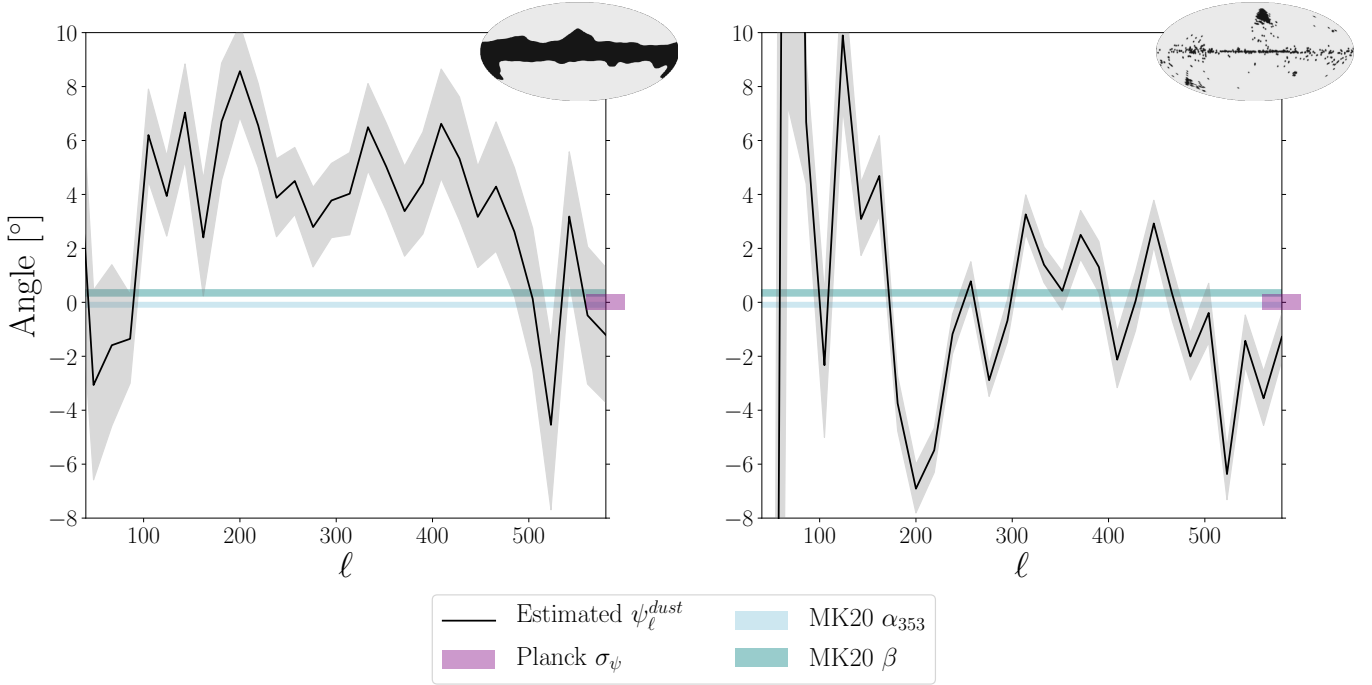


Figure 9. A comparison of our prediction for ψ_ℓ^{dust} , the effective magnetic misalignment angle, to values from the **MK20** analysis. Black line is the effective ψ_ℓ^{dust} calculated from the ratio of TB and TE at 353 GHz. Gray band indicates the propagated 1σ error. Left: ψ_ℓ^{dust} computed over the mask considered in this work ($f_{sky} \sim 0.69$, upper righthand corner). Right: the same analysis calculated with PR3 data over the 353 GHz masks used in MK20 (HM1 mask, with $f_{sky} \sim 0.92$, pictured in upper righthand corner). Light blue band indicates the MK20 value calculated for the polarization angle miscalibration at 353 GHz, $\alpha_{353} = -0.09^\circ \pm 0.11^\circ$. Teal band denotes the MK20 inference of the isotropic cosmic birefringence angle, $\beta = 0.35^\circ \pm 0.14^\circ$. Purple band indicates the Planck polarization angle calibration uncertainty, $\sigma_\psi = 0.28^\circ$.

microwave polarization experiments. If we further posit that the dust r_ℓ^{EB} is constant as a function of frequency, these values can be straightforwardly scaled with the dust SED to estimate the dust EB at any frequency.

To assess the implications of our work for the **MK20** result, we repeat our analysis over their sky masks. The **MK20** masks are constructed to exclude bad pixels in the PR3 maps and sightlines with bright CO emission. The masks have $f_{sky} \sim 0.92, 0.89$ for half mission (HM) splits 1 and 2, respectively: considerably less conservative than the $f_{sky} \sim 0.69$ mask used in our analysis, which excludes a larger fraction of the bright dust emission near the Galactic plane. The **MK20** masks are tailored for use with the Planck PR3 HM1 and HM2 data splits, so we repeat our analysis with those data, as well as with NPIPE A and B data splits. The choice of Planck data product does not change the computed TB power spectrum within the errors.

We find that TB is neither robustly nonzero nor uniformly positive over the **MK20** sky masks. Thus, we do not predict a uniform sign for ψ_ℓ^{dust} , nor C_ℓ^{EB} , over the ℓ range considered here. Figure 9 shows ψ_ℓ^{dust} for the **MK20** masks (righthand panel). For comparison, we plot the **MK20** inference of the isotropic cosmic birefrin-

gence angle (β) and simultaneously determined polarization miscalibration angle at 353 GHz (α_{353}). These quantities are of the same order, or smaller than, the effective magnetic misalignment angle.

The **MK20** analysis assumes that the intrinsic (physical) foreground $EB = 0$ in their likelihood analysis. Thus the **MK20** method effectively constrains $\beta - \gamma$, where β is the birefringence angle and γ parameterizes the intrinsic dust EB , with positive γ corresponding to positive EB . If we had inferred that the dust contribution to EB was positive over the **MK20** sky masks, our results would indicate that their measurement of β cannot be entirely due to dust, and that the inference of the significance of β must be a lower limit. There are two reasons that we cannot draw this conclusion for the **MK20** result. The most important is that the measured TB and inferred dust EB are not robustly positive over the **MK20** masks. Figure 9 demonstrates that the sign of ψ_ℓ^{dust} is not uniform over the range of scales that **MK20** use to infer β (in their case, $51 < \ell < 1500$).

The second reason is that the parameterization of the Galactic EB signal as $C_\ell^{EB,dust} = \frac{1}{2}\sin(4\gamma(\nu))(C_\ell^{EE,dust} - C_\ell^{BB,dust})$, where $\gamma(\nu)$ is an effective rotation angle, relies on the assumption that the

correlation ratio r_ℓ^{EB} is constant as a function of ℓ (Miyamoto et al. 2019). Is this assumption well-motivated in the misaligned filaments picture? On the one hand, it is reasonable to expect that magnetically misaligned filaments might be more or less prevalent at particular spatial scales in the ISM. On the other hand, preferred scales in the distribution of filaments could also introduce a scale dependence in quantities like EE/BB , and this has not been observed within observational constraints. It could be that scale dependence exists in the E and B emission from filamentary structures, but this is washed out in the observed EE/BB by the emission from the rest of the ISM, i.e., the diffuse dust not in filaments.

Empirically, we find that over our fiducial sky mask, r_ℓ^{TB} and our inferred r_ℓ^{EB} are fairly constant over $100 \lesssim \ell \lesssim 500$. This is not the case, however, for the MK20 sky area. If r_ℓ^{EB} has a measurable scale dependence, the foreground EB signal is no longer degenerate with a global polarization angle miscalibration in the MK20 formalism. The scale dependence of the Galactic EB , in addition to its frequency dependence, may then be useful for disentangling this foreground signal from an isotropic cosmic birefringence angle. In this case the foreground EB contribution, whether estimated from the dust TB and TE via our formalism or otherwise, should be included explicitly in the likelihood analysis. As we have shown that the intrinsic Galactic EB is non-negligible, one may expect that the likelihood results will change upon making this correction; the exact shift cannot be predicted without a detailed treatment.

The comparison in Figure 9 highlights the importance of the sky mask for interpreting the foreground contribution to measurements of cosmic birefringence. Based on our findings, one well-motivated strategy for searches for an isotropic cosmic birefringence angle is to build masks that restrict the Galactic emission to a single sign of TE and TB , in order to simplify the expectation for the foreground EB . Because TE is generally positive in the diffuse ISM, this approach motivates the exclusion of high-column density sightlines that carry a reasonable astrophysical expectation of a negative TE signal (e.g., Bracco et al. 2019b). Otherwise, the anticorrelation between TB and EB in regions where $TE < 0$ will complicate estimation of the global EB signal that relies on TB and TE .

Our findings motivate application of the MK20 method to the fiducial mask considered here, or similar sky masks where our method predicts a uniformly-signed Galactic EB signal. Our results can also be used to estimate the foreground C_ℓ^{EB} directly over a given mask. Further investigation of the evidence for cosmic bire-

fringe using data from current and upcoming CMB experiments will be of great interest.

6. CONCLUSIONS

This paper demonstrates that the observed nonzero TB correlation is related to a misalignment between Galactic dust filaments and the plane-of-sky magnetic field. We summarize our key findings below.

1. In agreement with previous analyses, we report a positive TB signal over the high Galactic latitude sky. We measure $TB > 0$ when B is derived from Planck NPIPE 353 GHz data and T is any of NPIPE I_{857} , I_{353} , or a HI4PI map of HI column density (Figure 1).
2. We hypothesize that the origin of nonzero TB in Galactic dust emission is a coherent misalignment between ISM dust filaments and the local magnetic field. We use the Clark & Hensley (2019) HI-based Stokes parameter maps, which predict the dust polarization angle based on the assumption that linear HI structures are aligned parallel to the local magnetic field. We rotate the Q_{HI} and U_{HI} maps by a fixed angle and cross-correlate the rotated maps with HI total intensity and with the unrotated Q_{HI} and U_{HI} maps. This exercise demonstrates that nonzero TB and EB can be generated from misalignments between filaments and the magnetic field (Figure 2).
3. We compute $\Delta\theta(\text{HI}, 353)$, the angular difference between θ_{HI} and the Planck 353 GHz maps (Figure 3). We hypothesize that the sign of $\Delta\theta(\text{HI}, 353)$ is predictive of the signs of TB and EB in Galactic dust emission.
4. We introduce a formalism to test our hypothesis. We compute cross-correlations of the Planck polarization data after rotating the Q_{353} , U_{353} values of about half of the pixels in the map by a random angle. This preserves the polarized intensity but destroys correlations associated with the polarization angles of the selected pixels. As a null test, we select the rotated pixels randomly, and find that the measured TB' signal of the rotated sky is $\lesssim TB$ of the unrotated sky, as expected. If the rotated pixels are instead selected based on the sign of $\Delta\theta(\text{HI}, 353)$, we find $TB' > TB$ with TB' strongly positive when we rotate pixels with positive $\Delta\theta(\text{HI}, 353)$, and $TB' < TB$ with TB' strongly negative when we rotate pixels with negative $\Delta\theta(\text{HI}, 353)$ (Figure 4). This confirms our hypothesis.

5. We further demonstrate that the sign of $\Delta\theta(\text{HI}, 353)$ is predictive of the sign of EB in Galactic dust (Figure 5).
6. We predict correlations for the relative amplitudes of TB , TE , and EB , and test these correlations in Planck data and in the Kim et al. (2019) synthetic dust polarization maps of MHD simulations (Figure 6). We find strong support for our predictions, particularly in the synthetic data, where we can isolate realizations of the sky with strong positive (negative) TE and observe the predicted positive (negative) correlation between EB and TB (Figure 7).
7. Our results strongly support magnetically misaligned ISM filaments as the physical origin of parity-odd signals in Galactic dust emission. Filaments are misaligned relative to the sky-projected magnetic field with either handedness, but a net preference over the sky for one sense of misalignment generates the observed net positive TB .
8. Our results can be used to predict the intrinsic dust EB signal, a critical quantity for searches for an isotropic cosmic birefringence angle. We use the Planck-measured TB and TE correlations at 353 GHz to parameterize a scale-dependent effective magnetic misalignment angle, $\psi_\ell^{dust} \sim 5^\circ$ for $100 \lesssim \ell \lesssim 500$ over our fiducial sky mask (Figure 9, lefthand panel). Taking the measured r_ℓ^{TB} at 353 GHz as an upper limit on $r_\ell^{EB, dust}$, this translates to an estimated intrinsic dust EB of $\langle D_\ell^{EB} \rangle \lesssim 2.5 \mu\text{K}_{\text{CMB}}^2$ at 353 GHz. Planck data are not sensitive enough to test this prediction, but the intrinsic dust EB is a good target for future experiments.
9. The intrinsic dust EB is highly mask-dependent. We repeat our analysis over the Minami & Komatsu (2020) sky mask, and find that neither the measured TB nor our predicted EB are constant in sign over the ℓ range considered (Figure 9, righthand panel). MK20 assume that the intrinsic dust $EB = 0$ in their primary analysis, but argue that a positive dust EB would increase the significance of their 2.4σ inference of a nonzero isotropic cosmic birefringence angle. Our results preclude this interpretation of their measurement as a lower limit because our inference of ψ_ℓ^{dust} over the MK20 mask is not robustly positive, and because we do not find

support for the implicit assumption that $r_\ell^{EB} \sim \text{constant}$, a necessary condition for the intrinsic dust EB to be degenerate with the isotropic cosmic birefringence angle.

10. Based on these findings, we suggest that future searches for cosmic birefringence should include the intrinsic dust EB directly in the model used for the likelihood analysis. Our results can be used to predict or constrain this foreground EB . Our results also motivate a careful choice of sky mask in order to simplify the interpretation.

Whether the sign of the preferred filament misalignment is an accident of our particular vantage point on the Galaxy, or reflects some parity violating physics of the ISM, remains an open question. This should be further explored both theoretically and observationally. The work presented here underscores the utility of HI observations in general, and the Clark & Hensley (2019) maps in particular, for deciphering the physical origin of signals in the Galactic polarized dust emission.

Software: astropy (Astropy Collaboration et al. 2013, 2018), Healpix (Górski et al. 2005), healpy (Zonca et al. 2019), matplotlib (Hunter 2007), NaMaster (Alonso et al. 2019), numpy (Oliphant 2015), pandas (McKinney 2010)

ACKNOWLEDGMENTS

We thank David Weinberg and Matias Zaldarriaga for insightful comments on earlier versions of this work. We thank Yuto Minami and Eiichiro Komatsu for sharing the sky masks used in their analysis. S.E.C. acknowledges support by the Friends of the Institute for Advanced Study Membership. C.-G.K. and B.S.H. acknowledge support from the NASA TCAN grant No. NNN17ZDA001N-TCAN. J.C.H. thanks the Simons Foundation for support. This work makes use of observations obtained with Planck (<http://www.esa.int/Planck>), an ESA science mission with instruments and contributions directly funded by ESA Member States, NASA, and Canada. HI4PI is based on observations with the 100-m telescope of the MPIfR (Max-Planck- Institut für Radioastronomie) at Effelsberg and the Parkes Radio Telescope, which is part of the Australia Telescope and is funded by the Commonwealth of Australia for operation as a National Facility managed by CSIRO. This research has made use of NASA’s Astrophysics Data System.

REFERENCES

Abazajian, K., Addison, G., Adshead, P., et al. 2019, arXiv e-prints, arXiv:1907.04473

Abazajian, K. N., Adshead, P., Ahmed, Z., et al. 2016, arXiv e-prints, arXiv:1610.02743

- Abitbol, M. H., Hill, J. C., & Johnson, B. R. 2016, *MNRAS*, 457, 1796
- Ade, P., Aguirre, J., Ahmed, Z., et al. 2019, *JCAP*, 2019, 056
- Ade, P. A. R., Arnold, K., Atlas, M., et al. 2015, *PhRvD*, 92, 123509
- Aiola, S., Calabrese, E., Maurin, L., et al. 2020, *JCAP*, 2020, 047
- Alonso, D., Sanchez, J., Slosar, A., & LSST Dark Energy Science Collaboration. 2019, *MNRAS*, 484, 4127
- Astropy Collaboration, Robitaille, T. P., Tollerud, E. J., et al. 2013, *A&A*, 558, A33
- Astropy Collaboration, Price-Whelan, A. M., Sipőcz, B. M., et al. 2018, *AJ*, 156, 123
- Benson, B. A., Ade, P. A. R., Ahmed, Z., et al. 2014, in *Society of Photo-Optical Instrumentation Engineers (SPIE) Conference Series*, Vol. 9153, Millimeter, Submillimeter, and Far-Infrared Detectors and Instrumentation for Astronomy VII, ed. W. S. Holland & J. Zmuidzinas, 91531P
- Berdugugin, A., Piirola, V., & Teerikorpi, P. 2004, *A&A*, 424, 873
- Berdugugin, A., & Teerikorpi, P. 2002, *A&A*, 384, 1050
- Berdugugin, A., Teerikorpi, P., Haikala, L., et al. 2001, *A&A*, 372, 276
- Bianchini, F., Wu, W. L. K., Ade, P. A. R., et al. 2020, *PhRvD*, 102, 083504
- BICEP2 Collaboration, Keck Array Collaboration, Ade, P. A. R., et al. 2017, *PhRvD*, 96, 102003
- . 2018, *PhRvL*, 121, 221301
- BICEP2/Keck Collaboration, Planck Collaboration, Ade, P. A. R., et al. 2015, *PhRvL*, 114, 101301
- Blackman, E. G. 2015, *SSRv*, 188, 59
- Boulanger, F., Abergel, A., Bernard, J. P., et al. 1996, *A&A*, 312, 256
- Bracco, A., Candelaresi, S., Del Sordo, F., & Brandenburg, A. 2019a, *A&A*, 621, A97
- Bracco, A., Ghosh, T., Boulanger, F., & Aumont, J. 2019b, *A&A*, 632, A17
- Brandenburg, A., & Subramanian, K. 2005, *PhR*, 417, 1
- Caldwell, R. R., Hirata, C., & Kamionkowski, M. 2017, *ApJ*, 839, 91
- Carroll, S. M. 1998, *PhRvL*, 81, 3067
- Choi, S. K., Austermann, J., Basu, K., et al. 2020a, *Journal of Low Temperature Physics*, 199, 1089
- Choi, S. K., Hasselfield, M., Ho, S.-P. P., et al. 2020b, *JCAP*, 2020, 045
- Clark, S. E. 2018, *ApJL*, 857, L10
- Clark, S. E., & Hensley, B. S. 2019, *ApJ*, 887, 136
- Clark, S. E., Hill, J. C., Peek, J. E. G., Putman, M. E., & Babler, B. L. 2015, *PhRvL*, 115, 241302
- Clark, S. E., Peek, J. E. G., & Miville-Deschênes, M. A. 2019, *ApJ*, 874, 171
- Clark, S. E., Peek, J. E. G., & Putman, M. E. 2014, *ApJ*, 789, 82
- Draine, B. T., & Weingartner, J. C. 1997, *ApJ*, 480, 633
- Dulaney, T. R., & Gresham, M. I. 2010, *PhRvD*, 81, 103532
- Flauger, R., Hill, J. C., & Spergel, D. N. 2014, *JCAP*, 2014, 039
- Górski, K. M., Hivon, E., Banday, A. J., et al. 2005, *ApJ*, 622, 759
- Gruppuso, A., Molinari, D., Natoli, P., & Pagano, L. 2020, *JCAP*, 2020, 066
- Hanany, S., Alvarez, M., Artis, E., et al. 2019, *arXiv e-prints*, arXiv:1902.10541
- Heiles, C. 2000, *AJ*, 119, 923
- Hensley, B. S., Zhang, C., & Bock, J. J. 2019, *ApJ*, 887, 159
- HI4PI Collaboration, Ben Bekhti, N., Flöer, L., et al. 2016, *A&A*, 594, A116
- Huffenberger, K. M., Rotti, A., & Collins, D. C. 2020, *ApJ*, 899, 31
- Hunter, J. D. 2007, *Computing in Science and Engineering*, 9, 90
- Jow, D. L., Hill, R., Scott, D., et al. 2018, *MNRAS*, 474, 1018
- Kalberla, P. M. W., & Haud, U. 2020, *arXiv e-prints*, arXiv:2003.01454
- Kamionkowski, M., Kosowsky, A., & Stebbins, A. 1997a, *PhRvL*, 78, 2058
- . 1997b, *PhRvD*, 55, 7368
- Kandel, D., Lazarian, A., & Pogosyan, D. 2017, *MNRAS*, 472, L10
- Kaufman, J. P., Miller, N. J., Shimon, M., et al. 2014, *PhRvD*, 89, 062006
- Keating, B. G., Shimon, M., & Yadav, A. P. S. 2013, *ApJL*, 762, L23
- Kim, C.-G., Choi, S. K., & Flauger, R. 2019, *ApJ*, 880, 106
- Kim, C.-G., & Ostriker, E. C. 2017, *ApJ*, 846, 133
- Krachmalnicoff, N., Carretti, E., Baccigalupi, C., et al. 2018, *A&A*, 618, A166
- Kritsuk, A. G., Flauger, R., & Ustyugov, S. D. 2018, *PhRvL*, 121, 021104
- Lenz, D., Hensley, B. S., & Doré, O. 2017, *ApJ*, 846, 38
- Martin, P. G., Blagrove, K. P. M., Lockman, F. J., et al. 2015, *ApJ*, 809, 153
- McClure-Griffiths, N. M., Dickey, J. M., Gaensler, B. M., Green, A. J., & Haverkorn, M. 2006, *ApJ*, 652, 1339

- McKinney, W. 2010, in *Proceedings of the 9th Python in Science Conference*, ed. S. van der Walt & J. Millman (Austin, TX: SciPy), 51 – 56
- Minami, Y., & Komatsu, E. 2020, *PhRvL*, 125, 221301
- Minami, Y., Ochi, H., Ichiki, K., et al. 2019, *Progress of Theoretical and Experimental Physics*, 2019, 083E02
- Murray, C. E., Peek, J. E. G., & Kim, C.-G. 2020, *ApJ*, 899, 15
- Naess, S., Aiola, S., Austermann, J. E., et al. 2020, *JCAP*, 2020, 046
- Namikawa, T., Guan, Y., Darwish, O., et al. 2020, *PhRvD*, 101, 083527
- Oliphant, T. E. 2015, *Guide to NumPy*, 2nd edn. (USA: CreateSpace Independent Publishing Platform)
- Page, L., Hinshaw, G., Komatsu, E., et al. 2007, *ApJS*, 170, 335
- Panopoulou, G. V., & Lenz, D. 2020, *ApJ*, 902, 120
- Peek, J. E. G., & Clark, S. E. 2019, *ApJL*, 886, L13
- Pelgrims, V., Clark, S. E., Hensley, B. S., et al. 2021, *A&A*, 647, A16
- Planck Collaboration I. 2020, *A&A*, 641, A1
- Planck Collaboration III. 2020, *A&A*, 641, A3
- Planck Collaboration Int. LVII. 2020, *A&A*, 643, A42
- Planck Collaboration Int. XIX. 2015, *A&A*, 576, A104
- Planck Collaboration Int. XLIX. 2016, *A&A*, 596, A110
- Planck Collaboration Int. XXX. 2016, *A&A*, 586, A133
- Planck Collaboration Int. XXXII. 2016, *A&A*, 586, A135
- Planck Collaboration Int. XXXV. 2016, *A&A*, 586, A138
- Planck Collaboration Int. XXXVIII. 2016, *A&A*, 586, A141
- Planck Collaboration IX. 2014, *A&A*, 571, A9
- Planck Collaboration XI. 2020, *A&A*, 641, A11
- Purcell, E. M. 1975, *Interstellar grains as pinwheels.*, ed. G. B. Field & A. G. W. Cameron, 155–167
- Rosset, C., Tristram, M., Ponthieu, N., et al. 2010, *A&A*, 520, A13
- Rotti, A., & Huffenberger, K. 2019, *JCAP*, 2019, 045
- Schlegel, D. J., Finkbeiner, D. P., & Davis, M. 1998, *ApJ*, 500, 525
- Seljak, U., & Zaldarriaga, M. 1997, *PhRvL*, 78, 2054
- Smith, K. M. 2006, *NewAR*, 50, 1025
- Soler, J. D., Ade, P. A. R., Angilè, F. E., et al. 2017, *A&A*, 603, A64
- Watanabe, M.-A., Kanno, S., & Soda, J. 2009, *PhRvL*, 102, 191302
- . 2011, *MNRAS*, 412, L83
- Weiland, J. L., Addison, G. E., Bennett, C. L., Halpern, M., & Hinshaw, G. 2020, *ApJ*, 893, 119
- Yadav, A. P. S., Su, M., & Zaldarriaga, M. 2010, *PhRvD*, 81, 063512
- Zaldarriaga, M. 2001, *PhRvD*, 64, 103001
- Zonca, A., Singer, L., Lenz, D., et al. 2019, *The Journal of Open Source Software*, 4, 1298